

Cr³⁺ spin dynamics under the octahedral crystal field in van der Waals antiferromagnets

Rabindra Basnet,¹ Subhashree Chatterjee,¹ Paul Kigaya,¹ Ezana Negusse,¹ J. van Tol,² and Ramesh C. Budhani^{1,*}

¹*Department of Physics, Morgan State University, Baltimore, MD, 21251, USA*

²*National High Magnetic Field Laboratory, Florida State University, Tallahassee, Florida 32310, USA*

Abstract

The magnetic moment in van der Waals (vdW) materials containing 3d transition metals originates from unpaired *d*-electron spins and their interaction with surrounding ligands. The interplay between exchange interactions and magnetic anisotropy stabilizes long-range ordering of such moments. The compound CuCrP₂S₆ (CCPS) presents an interesting class of vdW solids where the coupling of Cr³⁺ moments and ordering of Cu¹⁺ ions give rise to a multiferroic ground state. Here we investigate the spin dynamics of Cr³⁺ ions in CCPS through magnetization and broadband as well as single sub-THz magnetic resonance measurements. The orbital moment of Cr³⁺ is quenched under the octahedral crystal field of surrounding chalcogen ions, resulting in negligible magnetic anisotropy—a feature common to Cr-based vdW antiferromagnets (AFM). Resonance spectra over a wide frequency–field–temperature range reveal quasi-2D AFM dynamics governed mainly by isotropic Cr–Cr exchange interactions, which determine the magnetic order, spin reorientation, and damping. Sub-THz resonance spectra also uncover a field-induced ferromagnetic polarization, highlighting the universal role of Cr–Cr exchange in layered Cr compounds. Moreover, persistent magnetic correlations far above the Néel temperature ($T_N \approx 32$ K) points to short-range magnetic order in CCPS and motivates future studies of a possible interplay between AFM and antiferroelectric orders. These results establish CCPS as an exemplary system for exploring 2D magnetism and electric-field-tunable spintronic functionalities in layered multiferroics.

*ramesh.budhani@morgan.edu

I. INTRODUCTION

Magnetic materials are constructed from magnetic moments located on the atomic sites of a crystal lattice, where they interact through exchange interactions of Coulombic and dipolar character. These moments originate predominantly from the unpaired d - or f -electron spins of the ions, which determine their total moment as well as the nature and strength of exchange and anisotropy. Van der Waals (vdW) magnets have recently emerged as key platforms for studying low-dimensional magnetism and its technological applications [1,2]. Amongst the $3d$ metal cations in vdW magnets, materials based on Cr^{3+} ions have garnered significant attention due to their robust magnetic ordering from bulk to the monolayer limit [3–6]. Compounds such as CrI_3 [3] and $\text{Cr}_2\text{Ge}_2\text{Te}_6$ [4] were the first experimentally confirmed Cr-based 2D magnets. In general, Cr compounds are of great importance due to the plethora of rich magnetic phases they host. For example, $\text{Cr}(\text{Br},\text{I})_3$ [3,7–9] and $\text{Cr}_2(\text{Si},\text{Ge})_2\text{Te}_6$ [4,10] exhibit ferromagnetism (FM) while CuCrP_2S_6 [11–13], CrPS_4 [14], CrCl_3 [15], and CrSBr [16] are antiferromagnets (AFMs). These compounds possess octahedral (O_h) symmetry, with Cr^{3+} ions forming CrX_6 octahedra. The $3d^3$ electronic configuration of Cr^{3+} yields a half-filled t_{2g} manifold and empty e_g states, leading to strong orbital-moment quenching. As a result, spin-orbit coupling (SOC) and magnetocrystalline anisotropy are intrinsically weak, a feature often cited as the origin of the flexible magnetic ordering observed in such systems [17–22].

Furthermore, the half-filled t_{2g} configuration influences the nature of magnetic exchange pathways. It usually favors the direct d - d hopping, which typically promotes AFM coupling [23]. Nevertheless, the FM ordering also emerges in Cr systems, particularly those with heavier ligands [3,4,7–10]. While the Cr d -orbitals contribute similarly across all Cr-based vdW magnets, the key difference stems from the ligand p -orbitals, where anisotropic p - d superexchange dictates the nature of the magnetic ground state [19–21,24,25]. The magnetic exchange and anisotropy are sensitive to the SOC strength of p -electrons and the degree of p - d covalency [21], which depend on the chemical identity and spatial geometry of the coordinating ligands. This delicate balance between AFM and FM ground states is a distinctive feature in Cr^{3+} systems; and therefore, unraveling its microscopic origin necessitates further investigations, including the studies of spin dynamics over wider timescales.

Magnetic resonance spectroscopy is an ideal tool for studying magnetization dynamics [9,12,24,26–32]. These include ferromagnetic resonance (FMR) [9,24,27,29,31] and

electron paramagnetic/spin resonance (EPR/ESR) [26,27,30,32], which have been used to probe the magnetic order in Cr-based vdW compounds. Such studies demonstrate the 2D magnetic correlations [26,29,30,32] and the presence of multi-domain structures [9,31]. However, the earlier works have been limited to FM and paramagnetic (PM) resonances, primarily due to the high resonance frequencies of AFMs, which typically fall in the terahertz (THz) range, requiring advanced THz spectroscopies to access antiferromagnetic resonance (AFMR) [33,34]. Nonetheless, a few Cr-based magnets, such as CrCl_3 [28], CuCrP_2S_6 [12], and CrSBr [35], exhibit AFMR at relatively lower frequencies, within the typical microwave range. These studies have revealed strong magnon-magnon coupling in CrCl_3 [28] and the multiple magnon modes during the spin-flop (SF) transition in CuCrP_2S_6 [12].

In this work, we have studied the spin dynamics of Cr^{3+} ions subjected to an octahedral crystal field in the layered AFM compound CuCrP_2S_6 (CCPS) using magnetization and GHz frequency AFMR measurements. CCPS has attracted considerable interest recently for its multiferroic properties and robust magnetoelectric character extending down to the monolayer limit [36,37], making it important for exploring the coupling between magnetic and ferroelectric order parameters in two-dimensions. The temperature and field-dependent susceptibility measurements suggest orbital moment quenching of the Cr^{3+} ion, which is further confirmed by AFMR spectroscopy down to $T = 1.2$ K arising from the quasi-2D AFM dynamics of CCPS. The pronounced resonant absorption of microwaves across a broad frequency, temperature, and field (f - T - H) phase space reveals negligible anisotropy, indicating that the magnetic order, spin reorientation, and damping are primarily governed by the isotropic Cr-Cr exchange interactions. Moreover, the magnetization and high-frequency (240 GHz) FMR measurements uncover a field-induced FM-like spin polarization originating presumably from the intrinsic Cr-Cr interactions. These findings provide fresh insights into the fundamentals of magnetic ordering in vdW antiferromagnets, together with establishing a pathway for microwave control of AFM dynamics. Further, the evidence of room-temperature ferroelectricity in very thin platelets and the exceptionally low damping potentially make CCPS a promising vdW material for next-generation technological applications.

II. EXPERIMENT

The single crystals of CCPS used in this work were synthesized by chemical vapor transport (CVT) using iodine as the transport agent. First, ~ 1.2 g of the stoichiometric mixture of Cu (99.9%, Thermo Scientific), Cr (99.97%, Thermo Scientific), P (99%, Beantown Chemical), and S (99.99%, Thermo Scientific) together with 40 mg of I_2 (99.8%, Thermo Scientific) was sealed in an evacuated (pressure $\sim 10^{-5}$ Torr) quartz tube using an oxygen-acetylene torch. As shown in the inset of Fig. 2a, the millimeter-sized single crystals with flat and shiny surfaces were obtained after 1 week of CVT growth with a temperature gradient from 750 to 650°C. These crystals were characterized by X-ray diffraction (XRD) and Raman spectroscopy at room temperature. The XRD was performed using a Rigaku miniflex diffractometer with $Cu-K\alpha 1$ radiation. A typical diffraction pattern of the crystals placed such that the scattering vector is parallel to the c -axis has only the $(00L)$ reflections (Fig. 2a). The Raman measurement was conducted with an XploRA PLUS confocal Raman microscope (Horiba). The surface topography, thickness, ferroelectricity, and polarization switching of an exfoliated CCPS nanoflake on a Pt-coated Si substrate were studied using an NX10, Park Systems AFM at room temperature. The ferroelectric and piezoelectric characteristics were measured using a Pt/Cr coated conducting tip with a tip sensitivity of 33.33 V/ μm and a force constant of 3 N/m with an AC drive voltage of 1 V in off-Resonance piezoresponse force microscopy (OR-PFM) mode (17 kHz), throughout all the measurements. The magnetization measurements were performed in a physical property measurement system (PPMS EverCool). For the AFMR spectroscopy, a custom-built cryo-FMR spectrometer [38], which operates in the frequency modulation mode over a bandwidth of 1 to 22 GHz down to 1.2 K, has been used. The sample was placed on the U-shaped signal line of a grounded co-planar waveguide where the frequency-modulated GHz input from an RF source is fed, and the rectified return signal is measured using lock-in detection. The mutually perpendicular static and RF magnetic fields (H_{RF}) were along the sample plane (i.e., ab -plane) in these experiments. High-frequency EPR measurements were performed at the National High Magnetic Field Laboratory (NHMFL) located at Florida State University [26]. The sample was cooled down to 5 K under zero-field-cooling conditions to ensure the solidification of the vacuum grease used for mounting the sample. These experiments were conducted over the temperature range of 5 to 260 K, at 240 GHz excitation and a dc magnetic field aligned parallel to the ab -plane of the crystal. Measurements were also conducted at different field orientations from out-of-plane $\theta = 0^\circ$ to in-plane $\theta = 90^\circ$ directions at 10 K. The plate-like sample was mounted on a sample rotator, allowing

both temperature (at fixed angle) and angular-dependent (at fixed temperature) EPR measurements.

III. RESULTS AND DISCUSSION

A transition metal ion in free space exhibits full rotational symmetry $SO(3)$, resulting in five-fold degeneracy of its d -orbitals. However, this symmetry is lowered in a crystalline environment. In transition metal (M) based vdW materials, the M atoms typically form a planar honeycomb network within each layer and coordinate octahedrally with ligand chalcogen atoms (X) through edge-sharing octahedra. Therefore, despite distinct crystal structures, the vdW magnets often share a common structural motif, where each M atom is centrally positioned within an MX_6 octahedron, coordinated by four ligands in the basal plane and two in the out-of-plane direction, as shown in Fig. 1a. An ideal octahedron features six ligands equidistant from a central M atom. Under such octahedral coordination, the full rotational $SO(3)$ symmetry is reduced to the discrete symmetry group of the octahedra, represented as O_h . The crystal electric field created by the O_h symmetry of the transition metal cations lifts the five-fold degeneracy of the d -states, splitting it into lower-energy t_{2g} and higher-energy e_g orbitals. Among the five d -orbitals, the $d_{x^2-y^2}$ and d_{z^2} orbitals point directly towards the surrounding ligands (Fig. 1a). Consequently, the electrons in these orbitals experience greater electrostatic repulsion, pushing them to a higher energy level and creating a two-fold degenerate high-energy e_g orbital. On the other hand, the remaining three d -orbitals d_{xz} , d_{yz} , and d_{xy} do not directly align towards ligands (Fig. 1a), thus experiencing a weaker repulsion. This group of orbitals, commonly referred to as t_{2g} , which is three-fold degenerate, lies below the e_g orbitals [23,39]. This splitting of the five $3d$ orbitals under the octahedral crystal field is depicted in Fig. 1a. Table I highlights the fact that most Cr-based vdW magnets exhibit O_h symmetry with Cr^{3+} ion forming a CrX_6 octahedron with the surrounding ligands (Fig. 1a; left panel). In certain cases, such as in $CrSiTe_3$ [40] and $CrSBr$ [16], the octahedron is slightly distorted, where the out-of-plane ligands are often located at different distances from the central M atom than the in-plane ligands [23]. This further lowers the local point symmetry to D_{3d} (trigonal distortion) and D_{2v} (orthorhombic distortion), respectively. As mentioned earlier, the half-filled t_{2g} orbital for the Cr^{3+} ion under O_h symmetry typically favors AFM ordering [23]. However, in systems with heavier ligands, the enhanced covalency due to

greater orbital overlap facilitates FM superexchange interactions, ultimately stabilizing the FM ground state [19–21]. Hence, as presented in Table I, Cr compounds such as CCPS [11–13], $(\text{Ni}_{0.91}\text{Cr}_{0.09})\text{PS}_3$ [41], CrPS_4 [14], and CrCl_3 [15] containing lighter ligands exhibit an AFM ground state. In contrast, FM ordering emerges in systems with heavier ligands like Te, Br, and I. Even in AFM Cr compounds, the signatures of ferromagnetism are still evident. This delicate balance between the AFM and FM ground states, depending on the nature of the chalcogen, suggests a high propensity of the AFM state to a magnetic field–induced spin flop (SF) transition to the FM state. A conceptual schematic of this field–induced magnetic phase transition is depicted in Fig. 1b. However, this picture needs experimental verification and an in-depth analysis to uncover the mechanism responsible for such a phase transition in the Cr^{3+} –based vdW magnets.

Table I. *Magnetic properties of a few well-known Cr-based vdW antiferromagnets. In these materials, the Cr^{3+} ion is subjected to an octahedral (O_h) or distorted octahedral (D_{2v} or D_{3d}) crystal electric field arising from the coordination of surrounding ligands. Here, IP and OOP denote in–plane and out–of–plane directions, respectively.*

Materials	Crystal field symmetry	Magnetic structure	T_N/T_C (K)	B_{SF} (T)	B_S (T)	Ref.
CuCrP_2S_6	O_h	IP A-type AFM	~ 32	~ 0.4	~ 6.4	This work
$(\text{Ni}_{0.91}\text{Cr}_{0.09})\text{PS}_3$		IP AFM	~ 34	~ 0.6	~ 8.0	[41]
CrPS_4		OOP A-type AFM	~ 38	~ 0.7	~ 8.0	[14]
CrCl_3		IP A-type AFM	~ 14	~ 0.015	~ 0.25	[15]
CrBr_3		OOP FM	~ 37	NA	~ 0.20	[7,9]
CrI_3		OOP FM	~ 61	NA	~ 0.20	[8,9]
CrGeTe_3		OOP FM	~ 67	NA	~ 0.25	[61]
CrSiTe_3	D_{3d}	OOP FM	~ 33	NA	~ 0.40	[10,40,62]
CrSBr	D_{2v}	IP A-type AFM	~ 132	~ 0.3	~ 0.58	[16]

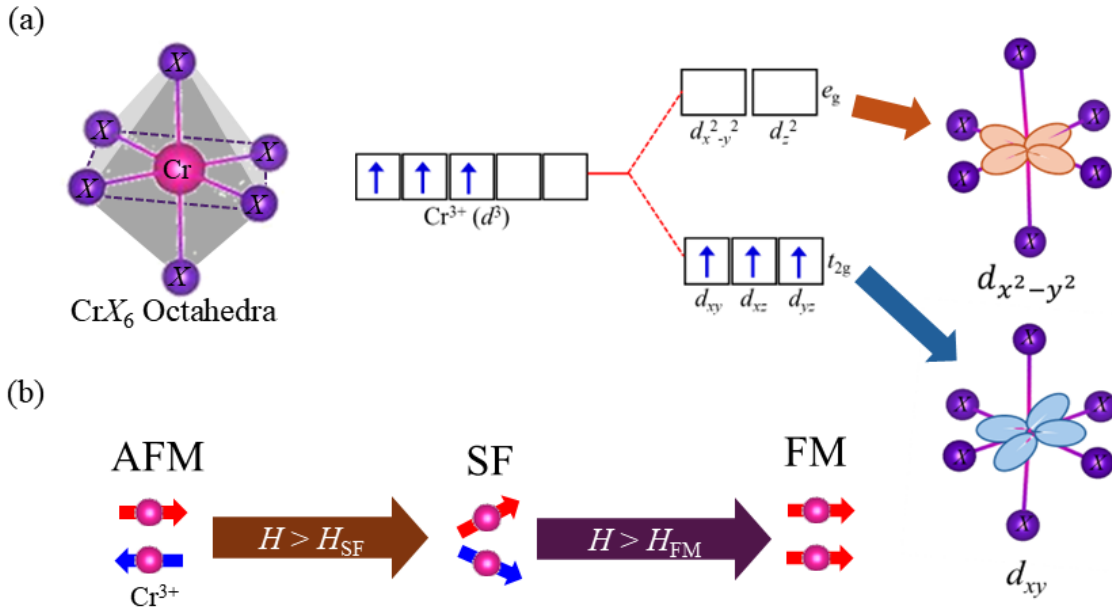


Figure 1. (a) Left panel: CrX_6 octahedron, where the pink and purple spheres denote Cr and X atoms. Here, X represents ligands such as chalcogen, halogen, etc. Right panel: Splitting of five 3d orbitals of Cr^{3+} cation into three t_{2g} and two e_g levels under an octahedral crystal field. The three 3d electrons of the Cr^{3+} ion occupy the lower t_{2g} orbitals, resulting in a half-filled configuration. The schematics also show the d_{xy} and $d_{x^2-y^2}$ orbitals with respect to the positions of the ligand atoms. (b) Conceptual schematic of the field-driven transition from AFM to SF state, followed by FM-like polarization of the Cr^{3+} moments.

With this motivation, we investigated the magnetic behavior of Cr^{3+} spin in vdW antiferromagnets, using CCPS as a representative material, which belongs to the metal thiophosphate (MPX_3) family of compounds. It is formed by replacing the bivalent metal ion M^{2+} with an equimolar ratio of monovalent Cu^{1+} and trivalent Cr^{3+} ions. Incorporating heterovalent metal ions in the formula adds chemical and structural complexity while maintaining charge neutrality in the system. Clearly, careful control of experimental conditions is essential to ensure successful crystal growth of this compound [11,42]. Fig. 2a (Inset) presents the optical microscope image of a millimeter-sized CVT-grown single crystal of CCPS, which exhibits a high-intensity (00L) XRD spectrum (Fig. 2a), consistent with the reported monoclinic ($C2/c$ space group) crystal structure [42]. Furthermore, room-temperature Raman measurement identifies four prominent modes, labeled I, II, III, and IV (Fig. 2b), that agree well with earlier Raman studies on CCPS [43,44]. These four peaks are assigned to the vibrational modes of Cu^{1+} and Cr^{3+} ions as

well as symmetric stretching and deformation of PS_3 units within the $(\text{P}_2\text{S}_6)^{4-}$ anions [44]. In CCPS, while the Cr^{3+} ions reside at the center of each sandwich layer within the vdW structure, the Cu^{1+} ions are off-centered along the c -axis [11,13,44,45] (Fig. 2c, left figure), breaking the inversion symmetry of the lattice and thereby inducing a spontaneous electric polarization in each layer even at ambient temperature [36]. To confirm the room-temperature ferroelectricity, we

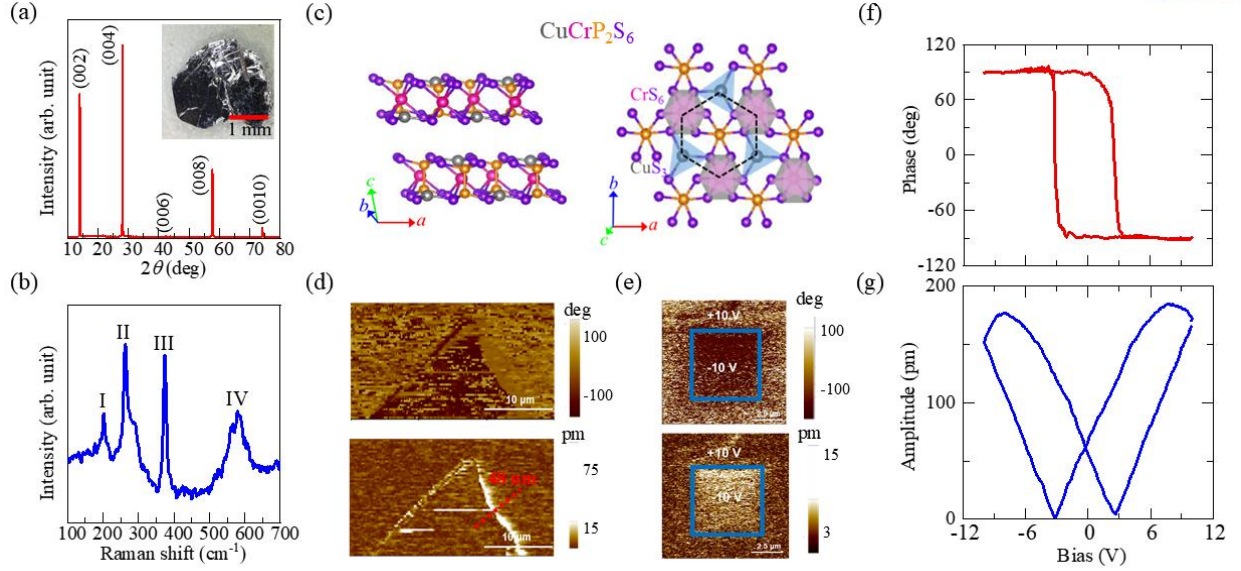


Figure 2. Growth and characterization of CCPS single crystal. (a) X-ray diffraction pattern of the CCPS crystal. Inset: The optical microscope image of a single crystal. (b) Raman spectra of the CCPS crystal at room temperature, showing four prominent peaks, labeled as I, II, III, and IV. (c) Left panel: The monoclinic crystal structure of CCPS showing a , b , and c axes. Right panel: The arrangement of Cu^{1+} and Cr^{3+} ions in a honeycomb network in the ab -plane (shown by the dashed hexagon), forming quasi-trigonal CuS_3 (blue triangles) and octahedral CrS_6 (magenta hexagon) units coordinated by S^{2-} ions. (d) PFM phase (upper panel) and amplitude (lower panel) images of a 48 nm-thick CCPS flake obtained by OR-PFM. (e) PFM phase (upper panel) and amplitude (lower panel) images acquired after writing a box-in-box pattern using a ± 10 V DC bias. (f) Off-field PFM phase hysteresis loop and (g) corresponding amplitude loop recorded during the DC bias switching process.

performed the PFM measurements on a thin (~ 48 nm) exfoliated CCPS flake shown in Fig. 2d. The corresponding PFM phase (Fig. 2d; upper panel) and amplitude (Fig. 2d; lower panel) images reveal clear ferroelectric domain contrast across the flake, indicating the presence of spontaneous polarization. To further probe the switchable polarization, a box-in-box pattern was written by applying a ± 10 V DC bias, as shown in the phase (Fig. 2e; upper panel) and amplitude (Fig. 2e;

lower panel) maps. The inner and outer regions exhibit opposite phase contrasts, confirming reversible domain switching under applied DC electric fields. The local ferroelectric switching behavior was also shown by measuring the off-field PFM phase hysteresis loop (Fig. 2f), which exhibits a 180° phase shift, a hallmark of ferroelectric polarization switching. The corresponding butterfly-shaped amplitude loop (Fig. 2g) displays the characteristic piezo-response of CCPS, with minima at the coercive voltages where polarization reversal occurs. These results collectively confirm the robust room-temperature ferroelectricity and switchable polarization in the CCPS flake.

Fig. 2c (right figure) illustrates the arrangement of Cu^{1+} and Cr^{3+} ions in a honeycomb network in the ab -plane (shown by the dashed hexagon), forming quasi-trigonal CuS_3 (blue triangles) and octahedral CrS_6 (magenta hexagon) units coordinated by S^{2-} ions. As discussed above, such an O_h symmetry of the Cr^{3+} ion has a significant impact on magnetism. To investigate the magnetic properties of CCPS, we have measured the temperature dependence of susceptibility (χ) under in-plane ($H // ab$) and out-of-plane ($H \perp ab$) magnetic fields of $\mu_0 H = 0.1$ T (Fig. 3a). The susceptibility of the CCPS single crystal exhibits a sharp PM to AFM transition with a Néel temperature T_N of ~ 32 K (black arrow, Fig. 3a), consistent with the earlier works [11–13,42]. The T_N peak is more pronounced in the in-plane susceptibility ($\chi_{//}$) compared to the out-of-plane (χ_{\perp}), and $\chi_{//}$ remains smaller than χ_{\perp} below T_N , indicating the in-plane easy axis in this compound. In fact, CCPS is found to possess an in-plane A-type AFM structure [12,46], with the Cr moments aligned ferromagnetically along the a -axis within each layer but forming AFM coupling between the adjacent layers (Fig. 3a, inset). Although this system adapts an AFM ground state, the magnetic order is primarily governed by intra-layer FM interactions, while inter-layer AFM interactions are rather weak [47]. This is supported by the positive Weiss temperature (Θ) obtained from the Curie-Weiss (CW) fitting of the susceptibility data, contrary to the negative Θ expected for AFM order. As shown by the red fitted line in Fig. 3b, χ in the PM state can be described by the CW law $\chi = \chi_0 + C / (T - \Theta)$, where χ_0 is the temperature-independent part of susceptibility and C is the Curie constant. The CW fitting yielded a value of $\Theta \approx (28.3 \pm 0.4)$ K, which is also confirmed by $1/\chi$ vs T plot (right vertical axis, Fig. 3b) and close to the reported values of $\Theta \approx 31.5$ K [46] and (35 ± 1) K [11], implying the dominant FM interactions in this material. Additionally, the CW coefficient C from the fit is $\approx (1.86 \pm 0.1)$ emu K / (Oe mol), which is used to estimate the effective moment (μ_{eff}) of the system using the relation $\mu_{\text{eff}} = \sqrt{(3K_B C / N_A)}$.

The strong FM correlation within the A-type AFM structure is further illustrated in the field dependence of magnetization [$M(H)$] measurements under $H // ab$ (upper panel) and $H \perp ab$ (lower panel) magnetic fields presented in Fig. 3c. Given the absence of magnetic hysteresis around zero field and the symmetric magnetization response in negative and positive field directions, we have only shown the $M(H)$ data from $\mu_0 H = 0$ to $+9$ T at all temperatures. CCPS exhibits a metamagnetic SF transition at an in-plane magnetic field of $\mu_0 H_{SF} \approx (0.44 \pm 0.06)$ T at $T = 5$ K, but is absent in the out-of-plane field direction, which is manifested as a clear upturn (shown by a red arrow in Fig. 3d) in isothermal $M(H)$ below T_N . The Cr-based vdW compounds undergo the SF transition at a relatively low field, typically below $\mu_0 H_{SF} < 1$ T (Table I). This behavior can be interpreted as the emergence of weak FM components, arising from the reorientation of spins from an AFM arrangement into a canted configuration when a field is applied along the easy axis. Applying a field exceeding H_{SF} spontaneously rotates the canted moments towards the field direction and eventually polarizes them above a saturation field (H_{FM}). This process is marked by the onset of field-independent magnetization near a saturation field of $\mu_0 H_{FM} \sim (6.4 \pm 0.4)$ T (blue arrow) and $\sim (7.8 \pm 0.4)$ T (purple arrow) in in-plane and out-of-plane magnetizations, respectively, at 5 K. Such a field-driven AFM to SF transition, followed by FM-like polarization at low field of just a few tesla, as depicted in Fig. 1b, appears to be a generic feature in AFM Cr compounds (Table I). The field-driven magnetic phase transition in CCPS is corroborated by the magnetic phase diagram shown in Fig. 3e, which summarizes the H_{SF} and H_{FM} critical fields extracted from the slope changes and kinks in the in-plane magnetization (easy axis), corresponding to the peak (red arrow) and sharp drop (blue arrow) in the derivative dM/dH (Inset, Fig. 3c). It also captures their temperature dependence below T_N , providing a comprehensive picture of the magnetic states over a wide field-temperature phase space in CCPS. Both the H_{SF} and H_{FM} fields reduce on approaching the T_N . The reduction of H_{FM} with the rising temperature is understandable. Here, thermal energy assists with moment reorientation, enabling polarization to occur at a lower field upon heating. On the other hand, the temperature dependence of H_{SF} is intriguing. While the suppression of H_{SF} has been seen in other Cr-based antiferromagnets, such as CrPS₄ [14] and CrSBr [16], this is in stark contrast to the opposite trend reported in other AFM compounds of this material family, such as MnPS₃ [48] and NiPS₃ [49], where it rises with temperature. The SF transition in these compounds is primarily governed by magnetic anisotropy rather than exchange interactions [49]. Therefore, the enhancement of H_{SF} with temperature may

originate from the temperature-induced modification of magnetic anisotropy. However, as mentioned earlier, the single-ion anisotropy for the Cr^{3+} ion is negligible. Thus, the moment rotation and the resulting SF transition in Cr-based AFM compounds are likely driven by a distinct mechanism, which will be discussed later in this work.

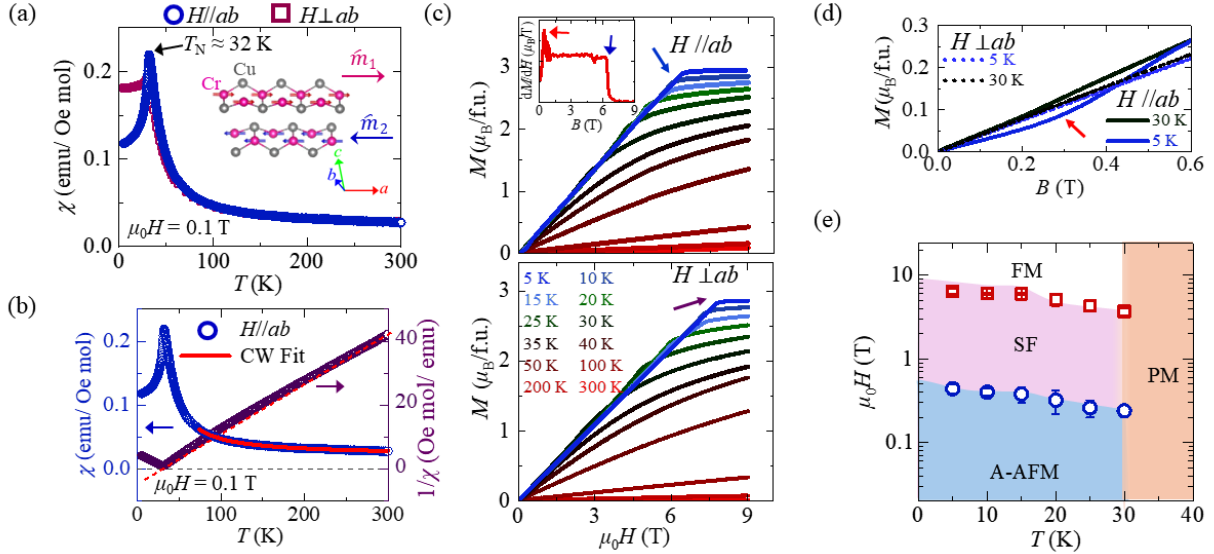


Figure 3. Magnetic properties of CCPS. (a) Temperature dependence of susceptibility (χ) for the sample under $H||ab$ and $H\perp ab$ fields of $\mu_0 H = 0.1$ T. The black arrow denotes the PM to AFM transition temperature $T_N \approx 32$ K. Inset: The magnetic structure of CCPS, where two AFM sublattices are represented by \hat{m}_1 and \hat{m}_2 . (b) Left vertical axis: The in-plane susceptibility data, reproduced from Fig. 3a, is shown with the Curie-Weiss (CW) fitting represented by the red curve. Right vertical axis: Inverse of susceptibility as a function of temperature. The red dashed line represents a linear regression of the high-temperature regime. (c) The $M(H)$ for CCPS sample under $H||ab$ (upper panel) and $H\perp ab$ (lower panel) magnetic fields from $T = 300$ to 5 K. Inset: The derivative dM/dH for $H||ab$ at $T = 5$ K at a field range of 0 to 9 T. The red and blue arrows denote H_{SF} and H_{FM} , respectively. (d) Zoom-in data of in-plane $M(H)$ below T_N to show the spin-flop transition (red arrow). Figs. 3c and 3d have the same color codes. (e) The magnetic phase diagram constructed from the in-plane $M(H)$ measurement presented in Fig. 3c.

In addition to the spin reorientation phenomenon, the absolute magnitude of magnetization in Cr-based compounds also present a notable point of interest. Studies based on magnetometry [11] and X-ray magnetic circular dichroism (XMCD) [50] have mainly attributed the net magnetic moment of such compounds to the Cr^{3+} spin, with a minimum contribution from orbital moment [11,50]. Similar magnetic behavior can also be seen in the magnetization

measurements of CCPS. At $T = 5$ K, the saturation magnetization for both field directions attains a value of $\sim 2.94 \mu_B$ per f.u., which is in good agreement with the spin-only moment of $g_S S \mu_B \approx 3 \mu_B$, where $g_S (\approx 2)$ is the free electron Landé g -factor and $S = 3/2$ for a Cr^{3+} ion. The Curie–Weiss analysis of susceptibility yields a $\mu_{\text{eff}} = (3.86 \pm 0.03) \mu_B$. This value aligns well with the theoretical result of $(\mu_{\text{eff}})_{\text{theo}} = g_S \sqrt{S(S+1)} \mu_B = 3.87 \mu_B$. These data suggest that the magnetic moment in CCPS originates predominantly from the spin-only contribution, implying a negligible orbital magnetic moment for a Cr^{3+} ion. This distinctive characteristic of Cr^{3+} ions placed in an octahedral crystal field is attributable to orbital moment quenching arising from their high-spin t^3_{2g} electronic configuration. Accordingly, these measurements serve primarily to benchmark our samples and establish a consistent framework for examining the Cr^{3+} spin dynamics with minimal orbital contributions.

Probing the magnetization dynamics may provide deeper insight into the unique magnetic behavior of Cr^{3+} spins. Here, we examine the AFM dynamics of CCPS using AFMR measurements performed across a range of temperatures and frequencies. The schematic in Fig. 4a depicts the Larmor precession and the fundamental concept behind the magnetic resonance phenomenon. The net magnetic moment of the spin system, given by the magnetization vector M (purple arrow), undergoes precessional motion around the applied static magnetic field H (red arrow), which is aligned perpendicular to the microwave magnetic field H_{RF} (orange double arrow). When the Larmor precession frequency of M matches that of the H_{RF} , resonance occurs, and the system absorbs microwave energy, resulting in a distinct change in microwave transmission or reflection. The microwave absorption in AFMR measurement is detected by scanning the DC magnetic field at a fixed excitation frequency. Owing to two anti-parallel magnetic sublattices in antiferromagnets, their precession dynamics involve coupled modes, and the subsequent resonance is relatively complex compared to the typical single-mode dynamics present in FMR. The nature of the AFMR in CCPS can be understood by studying the evolution of resonance as a function of input frequencies and modeling it with the coupled Landau–Lifshitz–Gilbert (LLG) equation, using a macrospin approximation for each spin sublattice [51]. This model assumes the uniform magnetization direction in two oppositely aligned magnetic sublattices 1 and 2, each with a magnitude of saturation magnetization M_S , which are denoted by the unit vectors \hat{m}_1 and \hat{m}_2 , respectively, as shown in the inset of Fig. 3a. The exchange forces are treated as molecular fields

$-H_E \hat{\mathbf{m}}_2$ and $-H_E \hat{\mathbf{m}}_1$ acting on the sublattices 1 and 2, respectively, where H_E is the interlayer exchange field. The coupled LLG equation, excluding damping, is given below:

$$\frac{d\hat{\mathbf{m}}_{1(2)}}{dt} = -\mu_0 \gamma \hat{\mathbf{m}}_{1(2)} \times [H - H_E \hat{\mathbf{m}}_{2(1)} - M_s (\hat{\mathbf{m}}_{1(2)} \cdot \hat{\mathbf{z}}) \hat{\mathbf{z}}] + \tau_{1(2)}, \quad (1)$$

where μ_0 is the permeability constant, γ is the gyromagnetic ratio, and $\hat{\mathbf{z}}$ is the direction perpendicular to the sample plane, i.e., along the crystallographic c -axis. τ_1 and τ_2 are the torques due to the microwave field on sublattices 1 and 2, respectively. When the magnetic field H is applied along the ab -plane, the above equation is symmetric under the combined symmetry operation of twofold C_2 rotation and sublattice exchange [28,35]. The two independent modes, namely optical and acoustic modes with opposite parity, emerge under such symmetry. Depending on the orientation of H and H_{RF} fields, these two modes co-exist or appear selectively in the resonance due to their different symmetry and coupling conditions. Prior work on the related

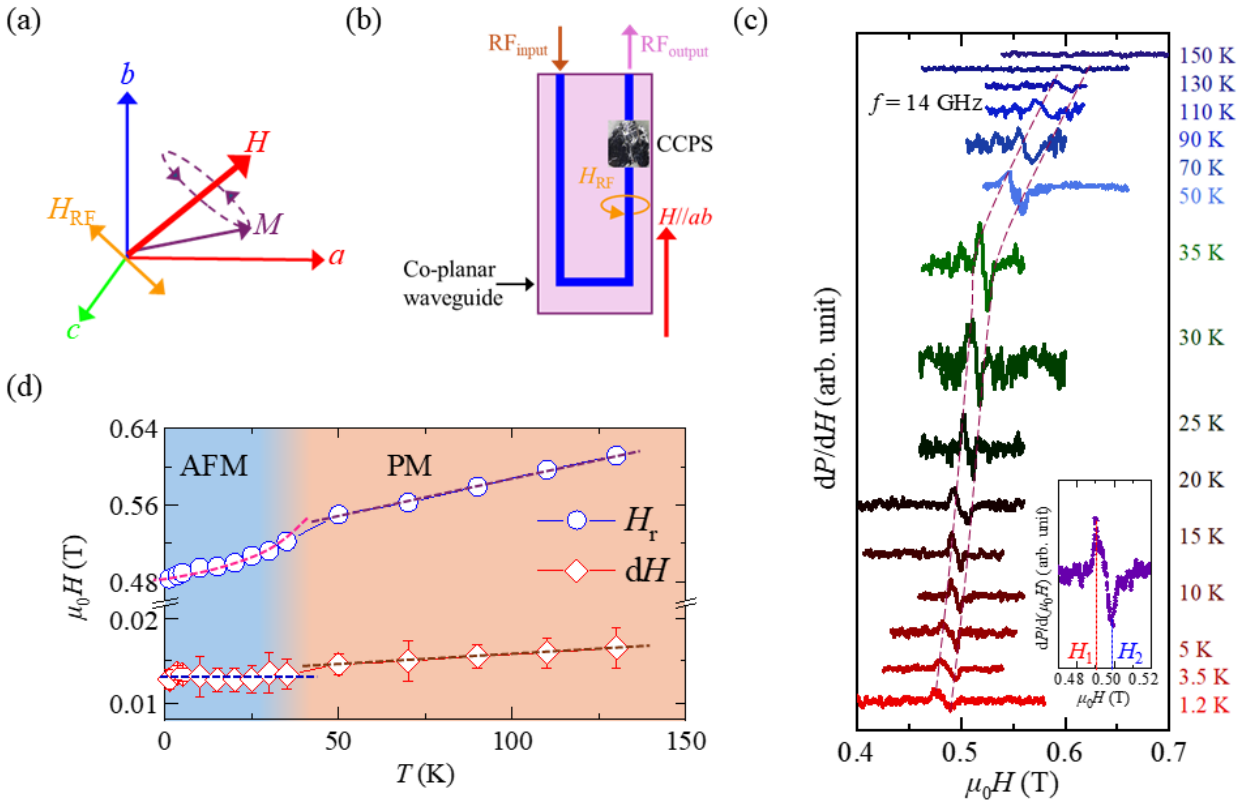


Figure 4. (a) A sketch of Larmor precession of magnetization (M) and orthogonality of the rf (H_{RF}) and dc (H) fields leading to magnetic resonance. Here, a , b , and c represent the crystallographic axes. (b) The grounded co-planar waveguide on which the crystal is glued with Apizone- N grease such that the ab -plane of the crystal is on the waveguide, and both H and H_{RF} fields lie within the ab -plane of a CCPS crystal. (c) The microwave absorption spectra of the CCPS single crystal, (d) Plot of the resonance field ($\mu_0 H_r$) and its derivative (dH) versus temperature (T).

recorded at $f = 14$ GHz over a temperature range of 1.2 to 130 K. Inset of Fig. (c) shows the method to extract the resonance field (H_r) and peak-to-peak linewidth (dH) of resonance. (d) Temperature dependence of H_r and dH across the PM and AFM phases. The dashed lines are a guide to the eye.

compound CrCl_3 has resolved both optical and acoustic modes of AFMR in the GHz frequency range when the H and H_{RF} fields are parallel [28]. In contrast, only the acoustic mode persisted under a perpendicular field configuration [28].

The experimental setup for the AFMR spectroscopy used here is illustrated in Fig. 4b. Both H and H_{RF} fields lie within the ab -plane of a CCPS crystal, yet oriented perpendicular to each other. As anticipated, a single resonance is detected for mutually perpendicular H and H_{RF} fields across the entire frequency range $f = 4 - 14$ GHz within the temperature interval $T = 1.2$ to 130 K. The typical absorption spectra recorded at $f = 14$ GHz and shown in Fig. 4c, reveal a single resonance mode persisting throughout the temperature range. The resonance field (H_r) and peak-to-peak linewidth (dH) of resonance are extracted following a standard method employed in earlier works [12,29,32]. The H_r has been defined as the midpoint between the peak (H_1 ; red dashed line) and valley (H_2 ; blue dashed line) positions of the field derivative of the absorbed power (dP/dH), as illustrated in the inset of Fig. 3c. Furthermore, the dH is given by $dH = (H_2 - H_1)$, reflecting the full width at half maximum of the Lorentzian absorption signal. The temperature dependence of H_r and dH is summarized in Fig. 4d. The resonance becomes undetectable on further heating above $T > 130$ K. The suppression of H_r on cooling under $H//ab$ field supports the in-plane magnetic easy axis in CCPS, consistent with the typical temperature-dependent H_r trend seen in other Cr-based antiferromagnets [27,30] and ferromagnets [29,52]. Notably, a pronounced change of slope of the H_r vs T plot occurs near the PM to AFM phase boundary. The H_r reduction continues from $\mu_0 H_r \approx 0.52$ T at 35 K to $\mu_0 H_r \approx 0.48$ T at 1.2 K. However, the change is not strictly linear with temperature below T_N (denoted by the dashed lines in Figs. 4c and d), suggesting the modulation of spin dynamics due to the onset of AFM ordering. Additionally, the dH also exhibits a distinct temperature dependence across the PM and AFM phases. The dH reduces linearly with decreasing temperature above T_N but displays a weaker temperature dependence upon entering the AFM phase (Fig. 3d). Indeed, contrasting temperature dependence of dH across the magnetic ordering temperature is commonly seen in other Cr compounds [26,30,52] as well. The microwave absorption below T_N in CCPS, where H_r is notably smaller than the H_{FM} field derived from $M(H)$

measurements (Fig. 3c), is likely associated with AFMR caused by its weak interlayer AFM coupling [28,35]. However, the persistence of resonance above T_N in these vdW materials is surprising. Previous studies have attributed this behavior either to PM resonance originating from localized Cr^{3+} ions [28] or to the presence of short-range magnetic correlation above the ordering temperature [27,30]. As summarized in Table II, the observation of a well-defined FMR/ESR signal extending to temperatures several times higher than T_N or T_C is a generic feature of Cr-based vdW magnets, with $T_{\text{SR}}/(T_N \text{ or } T_C)$ ranging from ~ 2 to ~ 12 . Importantly, the resonance at T_{SR} remains relatively narrow, with $dH(T_{\text{SR}})$ of only $\sim 10^{-1}$ – 10^{-2} T for most compounds, which points to robust short-range magnetic correlations that survive deep into the PM regime.

Table II. Summary of FMR/ ESR parameters for representative Cr-based AFM and FM compounds. Here, T_{SR} denotes the characteristic temperature up to which the FMR/ESR signal persists above the Néel temperature (T_N) or Curie temperature (T_C), reflecting the presence of short-range magnetic correlations. The ratio $T_{\text{SR}}/(T_N \text{ or } T_C)$ quantifies the relative extent of this correlated regime, while $dH(T_{\text{SR}})$ represents the FMR/ESR linewidth evaluated at T_{SR} .

Materials	T_{SR} (K)	$T_{\text{SR}}/(T_N \text{ or } T_C)$	$dH(T_{\text{SR}})$ (T)	Ref.
CuCrP_2S_6	130	~ 4.1	~ 0.016	This work
CrCl_3	175	~ 12.5	–	[27]
CrBr_3	300	~ 8.1	~ 0.03	[52]
CrGeTe_3	298	~ 4.4	~ 0.45	[29]
CrSBr	298	~ 2.2	~ 0.03	[30]

Deeper insights into the AFM dynamics of CCPS can be achieved by analyzing the variation of H_r with applied microwave frequency f . The $f(H_r)$ function extracted from AFMR measurements at various temperatures is presented in Fig. 5a. As described by the LLG equation (eq. 1), this behavior can be expressed by the following relation [28,51]:

$$f = \mu_0 \gamma' [\sqrt{\{2H_E(2H_E + M_s)\}}] H_r / 2H_E, \quad (2)$$

where γ' is the reduced gyromagnetic ratio ($\gamma' = |\gamma|/2\pi$). To verify the extent of orbital moment quenching and confirm that the net magnetic moment originates primarily from the spin-only value of the Cr^{3+} ion, the γ' below T_N is evaluated by fitting f as a function of H_r using eq. 2. This quantity allows for the calculation of the Landé g -factor (g) via the relation $g = |\gamma| \hbar / \mu_B$. On the

other side, in the PM regime, where the magnetization is proportional to the applied field, i.e., $M = \chi(T)H$, the resonant frequency is given by [28]:

$$f = \mu_0\gamma'[\sqrt{1 + \chi(T)}]H, \quad (3)$$

which is employed to fit the f vs H_r data above T_N . These fittings yielded a value of γ' between $\sim(28.80 \pm 0.13)$ GHz/T and $\sim(27.56 \pm 0.26)$ GHz/T within the temperature range of $T = 1.2$ to 130 K. A comparable value of $\gamma' \approx 28$ GHz/T has been reported for CrCl_3 [28,32], implying a similar AFMR dynamics for the Cr^{3+} ion. We estimated the g -value using γ' and plotted its evolution with temperature in Fig. 5b. Interestingly, the g -factor exhibits a weak temperature dependence and

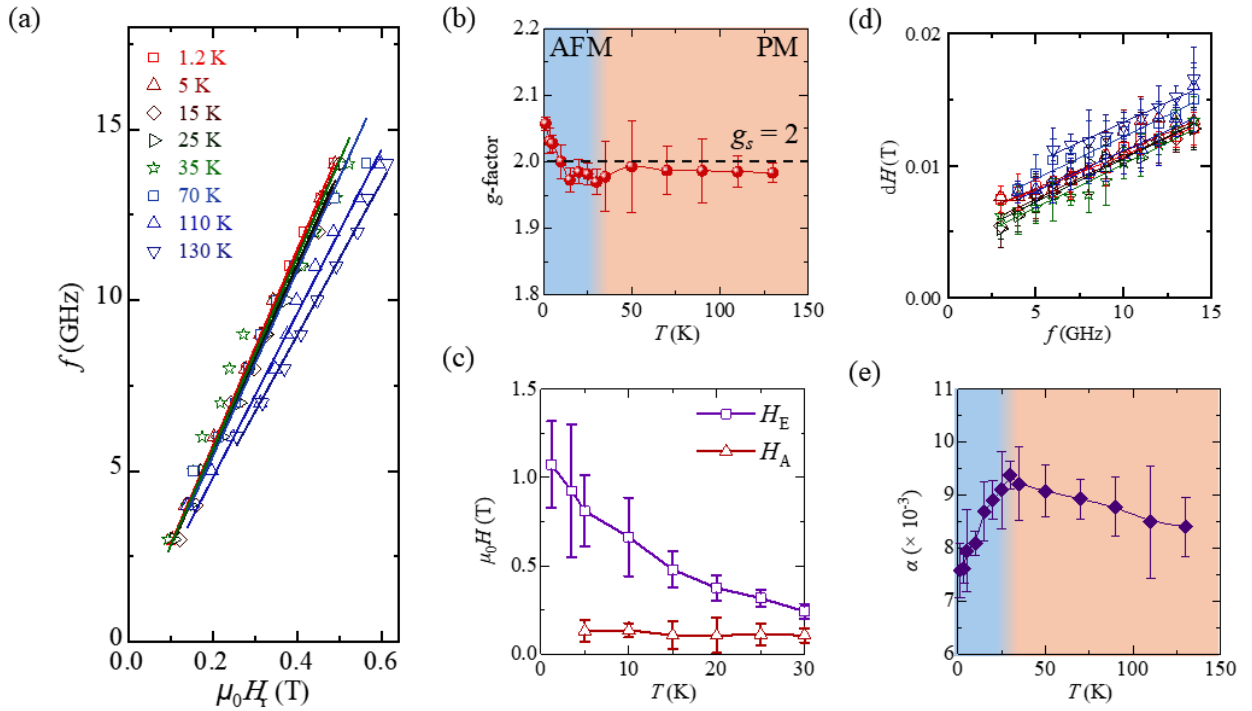


Figure 5. (a) Input frequency (f) as a function of resonance field H_r plotted at several temperatures in the range of 1.2 to 130 K for a CCPS crystal with its ab -plane parallel to the directions of the dc and RF fields. The solid lines indicate fitting of f vs H_r to a function presented in equation 2 (main text). (b) Temperature dependence of the Lande g -factor (g) across the PM and AFM states. The dashed line represents the spin-only g -factor $g_s = 2$. (c) Temperature dependence of the exchange (H_E) and effective anisotropy (H_A) fields below T_N . (d) The linewidth (dH) as a function of f over a temperature range of 1.2 to 130 K. The solid lines indicate fitting of dH vs f to a function presented in equation 4 (main text). The figures 5a and 5d use the same color codes. (e) Temperature dependence of the Gilbert damping parameter (α). The different colored regions in Figs. 5b and 5e represent AFM (blue) and PM (orange) states.

attains a value between $\sim(2.06\pm 0.01)$ and $\sim(1.97\pm 0.02)$ across AFM and PM phases, which is close to the spin-only Landé g -factor $g_s \approx 2$. This indicates a negligible orbital contribution to the total magnetic moment, in agreement with the saturation magnetization and effective moment derived from magnetization measurements, which are close to the theoretical spin-only value for the high-spin Cr^{3+} ion ($S = 3/2$). Using similar AFMR spectroscopy, a comparable g -factor close to $g_s \approx 2$, irrespective of the crystallographic orientations, has been determined for related AFM compounds such as CrCl_3 [32] ($g \approx 1.989$ for $H//ab$ and $g \approx 1.982$ for $H\perp ab$) and CrSBr [30] ($g \approx 1.996\pm 0.001$, 2.003 ± 0.001 , and 1.966 ± 0.001 for $H//a$, $H//b$, and $H//c$, respectively). Meanwhile, significantly larger g -factors, i.e., $g = 2.18\pm 0.02$ for $H//ab$ and $g = 2.10\pm 0.01$ for $H\perp ab$ have been estimated for a Cr-based ferromagnet $\text{Cr}_2\text{Ge}_2\text{Te}_6$ using FMR measurement [31]. The deviation from the spin-only g -factor in $\text{Cr}_2\text{Ge}_2\text{Te}_6$ suggests a finite orbital contribution to the total magnetization. An orbital moment of 8% and 5% along the in-plane and out-of-plane directions, respectively, has been confirmed in this compound [31]. Such a non-negligible orbital contribution strengthens the SOC effects and consequently amplifies the magnetic anisotropy of the system. In fact, a sizeable magnetocrystalline anisotropy energy of $(0.48\pm 0.02)\times 10^6$ erg/cm³ (i.e., $\sim 0.082\pm 0.0034$) meV per formula unit has been reported for $\text{Cr}_2\text{Ge}_2\text{Te}_6$ [29]. Additionally, a similar FMR study on a related ferromagnet, CrI_3 , has also revealed a strong magnetic anisotropy originating from the anisotropic Kitaev interactions [24]. This pronounced anisotropy accounts for the direction-dependent g -factors observed in ferromagnetic $\text{Cr}_2\text{Ge}_2\text{Te}_6$ [31], in stark contrast to the nearly isotropic g -values reported for its AFM counterparts [30,32]. These observations highlight the distinct microscopic mechanisms that govern the AFM and FM orderings in Cr-based magnetic materials.

While the ferromagnets such as $\text{Cr}_2\text{Ge}_2\text{Te}_6$ [31] and CrI_3 [24] exhibit strong magnetic anisotropy, the extent to which this effect shapes the Cr-based AFM systems remains less clear. To address this, we determined the AFM exchange field H_E and the effective anisotropy field H_A for CCPS, thereby clarifying the relative roles of exchange interactions and anisotropy in Cr antiferromagnets. The H_E field is directly extracted from the f vs H_r fitting using eq. 2 (Fig. 5a). While analogous AFMR approaches have been successfully used to determine H_E in layered antiferromagnets such as CrCl_3 [28] and CrSBr [35], a direct experimental determination of H_E for CCPS has been notably absent to date. With this H_E parameter, the H_A field is calculated through the expression:

$$H_{\text{SF}} = \sqrt{2H_E H_A - H_A^2}, \quad (3)$$

where the spin-flop field H_{SF} in the temperature range of 5 to 30 K is derived from $M(H)$ measurements (Fig. 3c). As seen in Fig. 5c, the H_{E} enhances as the temperature is lowered, indicating a steady strengthening of exchange interactions due to reduced thermal fluctuations. The H_{A} likewise grows as the system is cooled, but its temperature dependence is weak, and the magnitude remains far below that of H_{E} across the full temperature interval. The much smaller H_{A} relative to H_{E} corresponds well with the orbital moment quenching and the resulting weak magnetic anisotropy for Cr-based antiferromagnets, as discussed earlier. Further, within the standard two-sublattice AFMR framework, the resonance frequency can be approximated as $\omega \propto \gamma\sqrt{(H_{\text{E}}H_{\text{A}})}$ [35]; therefore, the small anisotropy field H_{A} also naturally accounts for the comparatively low AFMR frequencies observed in CCPS as well as in CrCl_3 [28], despite a sizable exchange field H_{E} . However, the stronger H_{E} field in CCPS leads to higher resonance fields H_{r} at similar frequencies relative to the H_{r} of CrCl_3 [28]. In such cases where magnetic anisotropy is negligible, the H_{E} also becomes the dominant factor governing magnetic order; consequently, its magnitude scales directly with the ordering temperature. For instance, a considerably larger $\mu_0 H_{\text{E}} \approx (1.07 \pm 0.24)$ T at 1.2 K is estimated for CCPS ($T_{\text{N}} \approx 32$ K) compared to a value of $\mu_0 H_{\text{E}} \approx 0.105$ T measured in CrCl_3 with $T_{\text{N}} \approx 14$ K [28]. Furthermore, the exchange field for CCPS (~ 1 T) is significantly smaller than the value of $\mu_0 H_{\text{E}} \approx 100$ T calculated in a pioneering work by Kittel [53] for another Cr antiferromagnet, Cr_2O_3 , which has a much higher T_{N} (~ 314 K) [54] than CCPS. In addition to the ordering temperature, the spin reorientation and the resulting field-induced SF transition in CCPS are likely governed by exchange interactions rather than anisotropy. Fig. 3d shows that the H_{SF} systematically increases upon cooling and mirrors the behavior of H_{E} , suggesting that exchange interactions primarily drive the SF transition in CCPS. This underscores the dominant role of isotropic Cr–Cr exchange interactions in stabilizing the AFM order in CCPS, with magnetic anisotropy playing only a marginal role.

In 2D honeycomb AFM systems with weak SOC, such as CCPS, the damping primarily arises from the relaxation of the electron spin via the exchange field [55]. This relaxation process is quantified by the phenomenological Gilbert damping parameter (α), which is extracted by linearly fitting dH vs f curves shown in Fig. 4d using the following equation

$$dH = (4\pi/\gamma)\alpha f + dH_0, \quad (4)$$

where dH_0 represents the inhomogeneous linewidth contribution and the γ is the gyromagnetic ratio that was already evaluated by fitting f as a function of H_{r} using eq. 2. The temperature

dependence of the α is plotted in Fig. 5e. For CCPS, the α ranges between $\approx (7.5 \text{ to } 9.4) \times 10^{-3}$ over the temperature interval of 1.2 to 130 K. Notably, this α is comparable to other Cr compounds, $\text{Cr}_2\text{Ge}_2\text{Te}_6$ [56,57] and CrBr_3 [9]. Such ultra-low magnetic damping is attributed to the weak SOC originating from the quenched orbital moment of the Cr^{3+} ion ($g \approx 2$), which suppresses the spin-phonon scattering and subsequently reduces the transverse magnetization relaxation [9,56,57]. Furthermore, because electrons are localized in an insulating system like CCPS, spin relaxation via electron-electron scattering is also weaker compared to that in conductive systems [9,56,57]. This highlights the robustness of spin coherence in such vdW semiconductors. Furthermore, the evolution of α with temperature is also intriguing; it increases upon heating from 1.2 K until reaching a maximum value near the PM-AFM phase boundary (Fig. 5e). This behavior can be ascribed to enhanced spin fluctuations promoting damping in the vicinity of the magnetic phase transition [58]. Further increasing the temperature reduces α before vanishing above $T = 130$ K. The persistence of damping even after the long-range magnetic order vanishes above T_N is intriguing. As mentioned earlier, the short-range magnetic correlations well beyond T_N [27,30] may lead to correlated spin clusters that can support collective spin excitations [59,60], giving rise to spin relaxation and finite damping even in the PM phase.

The dominant role of Cr-Cr spin interactions is further highlighted by the characteristic field-driven AFM-FM transition commonly observed in Cr-based antiferromagnets. As discussed earlier, these materials display a generic feature of field-induced FM-like saturation (Fig. 1b), which is also evident in the $M(H)$ measurements of CCPS (Fig. 3c). Although CCPS exhibits weak magnetic anisotropy, the isothermal magnetization still shows anisotropic features, manifested by the spin-flop transition only along the ab -plane and the direction-dependent saturation fields (Fig. 3c). However, upon full saturation, the magnetization becomes isotropic, reflecting the underlying isotropic Cr-Cr exchange interactions that govern the behavior of Cr^{3+} moments. Such nearly isotropic magnetic behavior is likewise reflected in the high-field magnetic resonance response. Applying the field $H > 2H_E$ drives the system into the FM state [28], where the LLG equation (eq. 2) is transformed to the Kittel formula, $f = \mu_0\gamma'[\sqrt{\{H(H + M_s)\}}]$ and the associated AFMR evolves into a uniform FMR mode characteristic of ferromagnets. For CCPS, the H_E is close to ~ 1 T, implying that FMR can be accessed for applied fields $\mu_0H_E > 2$ T. However, magnetic resonance spectroscopy could not be performed at such high fields due to the limited frequency range of our cryo-FMR spectrometer [38]. To overcome this, we carried out complementary high-frequency

FMR measurements at $f = 240$ GHz across a temperature range $T = 5$ –261 K (Fig. 6a) under $H // ab$ field configuration using the high-frequency EPR facilities at the NHMFL. To date, high-frequency FMR investigations have focused primarily on Cr-based vdW FM compounds such as CrBr_3 [26] and $\text{Cr}_2\text{Ge}_2\text{Te}_6$ [29] with only limited reports on related antiferromagnets such as CrCl_3 [27], and none to our knowledge for CCPS. At high temperatures, a single PM signal with

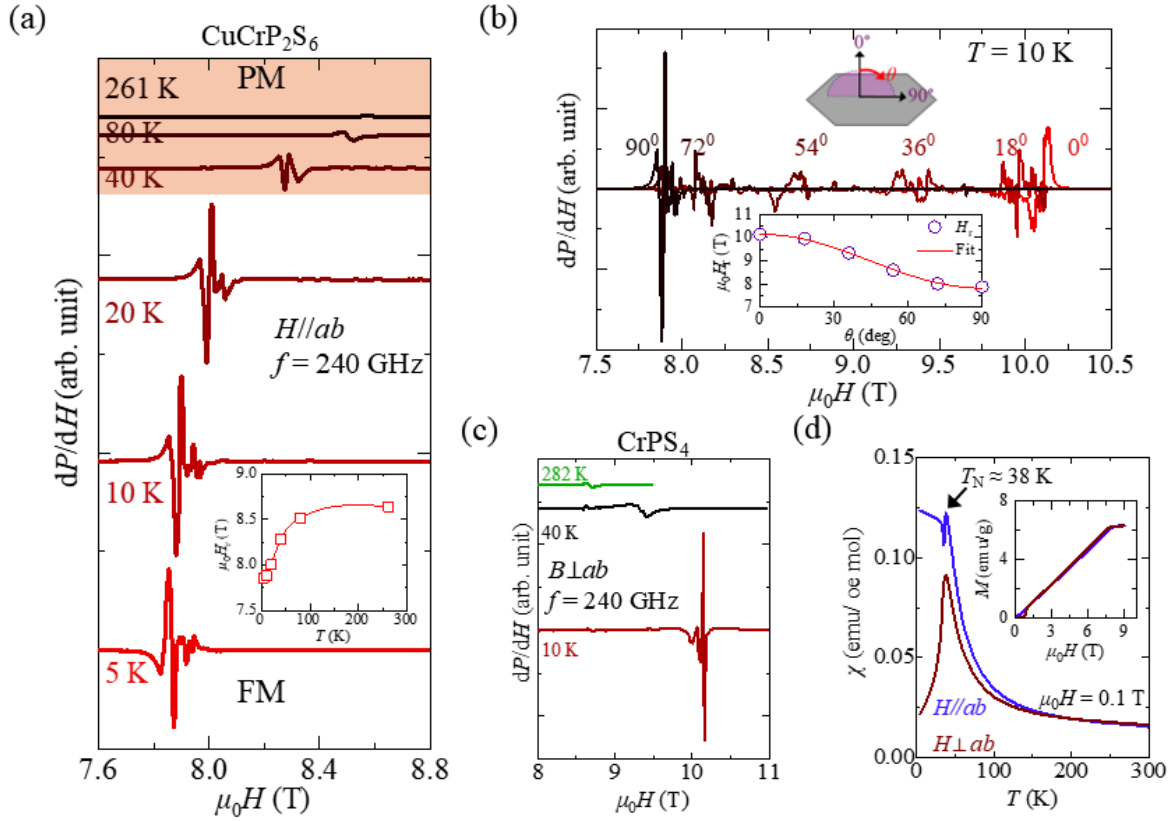


Figure 6. (a) The FMR spectra of a CCPS single crystal, recorded at 240 GHz over a temperature range of 5 to 261 K under the $H // ab$ applied field. Inset: Temperature dependence of H_r . (b) The FMR spectra of the CCPS crystal at 240 GHz and 10 K under various field orientations from out-of-plane ($\theta = 0^\circ$) to in-plane ($\theta = 90^\circ$) directions. Inset: Angular dependence of H_r , which is fitted by the equation: $H_r(\theta) = A(3\cos^2\theta - 1) + D$ (red solid line). (c) The FMR spectra of the CrPS_4 single crystal, recorded at 240 GHz and $T = 10, 40,$ and 282 K under the $H \perp ab$ field. (d) Temperature dependence of susceptibility (χ) for the CrPS_4 sample under $H // ab$ and $H \perp ab$ magnetic fields of $\mu_0 H = 0.1$ T. The black arrow denotes the $T_N \approx 38$ K. Inset: $M(H)$ for the CrPS_4 sample under $H // ab$ and $H \perp ab$ magnetic fields from $T = 10$ K.

a Lorentzian line shape is observed in CCPS (Fig. 6a). As the system approaches T_N , this signal progressively splits into multiple features. At such high frequencies, the resonance spectra correspond to FMR. Therefore, the low-temperature regime below T_N can be regarded as a high-frequency (or high-field) ferromagnetic state, hereafter denoted as FM (Fig. 6a). The multiple peaks in the high-frequency (240 GHz) FMR signal are also observed in CrBr₃ [26], which can be caused by several factors, including magnetocrystalline anisotropy, magnetic inhomogeneity, and magnetic phase separation [26]. Furthermore, strong absorption near resonance induces a rapid frequency dependence of the refractive index (n), causing symmetric phase shifts and interference effects. For typical dielectrics or semiconductors with $n \approx 2$ at microwave frequencies, the half-wavelength ($\lambda/2$) inside the material for a 240 GHz wave is approximately 300 μm , comparable to the sample thickness and thus enhancing these effects. Finite-size and surface deviations from an ideal thin plate further complicate the spectral structure. The temperature dependence of H_r is summarized in Fig. 6a (inset), which decreases on lowering the temperature, consistent with the AFMR results in Fig. 3d, and confirms the in-plane magnetic easy axis in CCPS. This easy-axis alignment along the ab -plane is further verified by angle-dependent FMR measurements at $T = 10$ K. As shown in Fig. 5b, FMR spectra were recorded for field orientations varying from $\theta = 0^\circ$ (out-of-plane) to $\theta = 90^\circ$ (in-plane), with the measurement geometry illustrated in the inset. With increasing angle θ , H_r systematically shifts to lower values, reaching its maximum in the out-of-plane configuration and minimum in the in-plane direction, in excellent agreement with the in-plane moment orientation in CCPS. Furthermore, the H_r as a function of θ angle is fitted using the model: $H_r(\theta) = A(3\cos^2\theta - 1) + D$ (red solid line). Such $(3\cos^2\theta - 1)$ dependence of H_r is a characteristic signature of 2D magnetic systems and has been reported in high-frequency FMR studies of CrBr₃ [26] and Cr₂Ge₂Te₆ [29]. This behavior further corroborates the AFMR and FMR arising from the quasi-2D magnetic dynamics of CCPS. Assuming the demagnetizing factors for an infinitely thin platelet ($N_x = N_y = 0$ and $N_z = 1$), the demagnetizing field (H_d) at the Cr sites is estimated to be ~ 1.43 T from the FMR relation: $f = (g\mu_B/h)(H_r - H_d)$, using an applied frequency of $f = 240$ GHz, the out-of-plane resonance field $\mu_0 H_r \approx 10$ T (Fig. 6b), and $g \approx 2$. For a uniform CCPS sample, the H_d should be equal to its volume magnetization (Magnetic moment/Unit cell volume) ≈ 0.12 T, using $\mu_{\text{eff}} \approx 3.86 \mu_B$ obtained from CW fitting (Fig. 3b) and unit cell volume $\approx 782 \text{ \AA}^3$ [11]. However, the substantially larger H_d field observed here indicates enhanced local

dipolar interactions arising from the layered structure, consistent with the quasi-2D magnetic nature inferred from the FMR and AFMR results.

The resonance fields in CCPS span from $\mu_0 H_r \approx 8$ T along the magnetic easy axis to ~ 10 T along the hard axis at $T = 10$ K (Fig. 5b). Furthermore, $\mu_0 H_r \approx 8$ T is consistently observed below T_N in the temperature interval $T = 5\text{--}20$ K (Fig. 5a). Comparable resonance fields at similar frequencies have been reported in related Cr-based systems, including CrCl_3 [27], CrBr_3 [26], and $\text{Cr}_2\text{Ge}_2\text{Te}_6$ [29]. Taken together, these results point to a generic physical origin that governs the field-driven AFM-to-FM transition in Cr antiferromagnets. To further clarify whether Cr-Cr exchange interactions are the underlying mechanism, we also carried out high-frequency FMR measurements at $T = 10, 40,$ and 282 K on a related antiferromagnet, CrPS_4 (Fig. 6c). This compound was chosen because the Cr^{3+} ions reside in an approximately O_h symmetric environment (Table I) and the absence of heavier ligands minimizes additional sources of magnetic anisotropy. In other words, CrPS_4 most likely captures the intrinsic magnetic behavior of Cr^{3+} moments and thus provides a meaningful comparison to CCPS. The magnetization measurements reveal $T_N \approx 38$ K for CrPS_4 (Fig. 6d), consistent with earlier works [14,22]. As the system is cooled below T_N , χ_\perp drops sharply in comparison to χ_\parallel , indicating the out-of-plane easy axis in this compound. This is confirmed by the metamagnetic SF transition in out-of-plane magnetization, accompanied by its smaller saturation field than that of in-plane magnetization (inset; Fig. 6d). Therefore, the FMR spectra for this compound were collected under the $H \perp ab$ field. The high-temperature resonance measurement reveals a single PM Lorentzian signal, while, as expected, multiple features emerge at $T = 10$ K (Fig. 6c). Notably, we obtain $\mu_0 H_r \approx 10.2$ T for the out-of-plane direction, which is in excellent agreement with the corresponding value observed in CCPS (Fig. 6b). The identical FMR behavior observed in two distinct Cr-based antiferromagnets suggests similar local dipolar interactions, further underscoring the universality of Cr-Cr exchange interactions as the fundamental microscopic mechanism that dictates AFM order and drives the field-induced AFM-FM transition in vdW Cr compounds.

In conclusion, we have investigated the Cr^{3+} spin dynamics of the vdW antiferromagnet CuCrP_2S_6 through magnetization, broadband AFMR, and high-frequency FMR measurements. Our study reveals that the magnetic behavior of CCPS is governed predominantly by isotropic Cr-Cr exchange interactions, while orbital moment quenching minimizes the influence of magnetic anisotropy. These fundamental interactions dictate the magnetic order, spin reorientation, and

magnetic damping, while enabling field-induced FM-like polarization. A key result of this investigation is the establishment of the universality of the magnetic behavior of several Cr^{3+} ion-based vdW AFM compounds. Collectively, CCPS emerges as a prototypical vdW antiferromagnet with microwave-tunable AFM dynamics, ultra-low damping, and possible room-temperature ferroelectricity, offering a promising platform for next-generation spintronic applications. Future investigations of a possible coupling between AFM and antiferroelectric order parameters may help elucidate potential magnetoelectric correlations and guide the design of multifunctional vdW materials.

Acknowledgements

This work at Morgan State University has been funded by the Department of Defense through grant # W911NF2120213. The contribution of J. V. Tol was funded by the NHMFL and National Science Foundation Cooperative Agreement No. DMR-2128556* and the State of Florida.

References

- [1] S. Wei, X. Liao, C. Wang, J. Li, H. Zhang, Y.-J. Zeng, J. Linghu, H. Jin, and Y. Wei, Emerging intrinsic magnetism in two-dimensional materials: theory and applications, *2D Mater.* **8**, 012005 (2020).
- [2] K. S. Burch, D. Mandrus, and J.-G. Park, Magnetism in two-dimensional van der Waals materials, *Nature* **563**, 47 (2018).
- [3] B. Huang et al., Layer-dependent ferromagnetism in a van der Waals crystal down to the monolayer limit, *Nature* **546**, 7657 (2017).
- [4] C. Gong et al., Discovery of intrinsic ferromagnetism in two-dimensional van der Waals crystals, *Nature* **546**, 265 (2017).
- [5] X. Cai et al., Atomically Thin CrCl₃: An In-Plane Layered Antiferromagnetic Insulator, *Nano Lett.* **19**, 3993 (2019).
- [6] D. R. Klein et al., Probing magnetism in 2D van der Waals crystalline insulators via electron tunneling, *Science* **360**, 1218 (2018).
- [7] M. Abramchuk, S. Jaszewski, K. R. Metz, G. B. Osterhoudt, Y. Wang, K. S. Burch, and F. Tafti, Controlling Magnetic and Optical Properties of the van der Waals Crystal CrCl₃-xBrx via Mixed Halide Chemistry, *Advanced Materials* **30**, 1801325 (2018).
- [8] M. A. McGuire, H. Dixit, V. R. Cooper, and B. C. Sales, Coupling of Crystal Structure and Magnetism in the Layered, Ferromagnetic Insulator CrI₃, *Chem. Mater.* **27**, 612 (2015).
- [9] X. Shen et al., Multi-domain ferromagnetic resonance in magnetic van der Waals crystals CrI₃ and CrBr₃, *Journal of Magnetism and Magnetic Materials* **528**, 167772 (2021).
- [10] T. J. Williams, A. A. Aczel, M. D. Lumsden, S. E. Nagler, M. B. Stone, J.-Q. Yan, and D. Mandrus, Magnetic correlations in the quasi-two-dimensional semiconducting ferromagnet CrSiTe₃, *Phys. Rev. B* **92**, 144404 (2015).
- [11] S. Selzer et al., Crystal growth, exfoliation, and magnetic properties of quaternary quasi-two-dimensional CuCrP₂S₆, *Phys. Rev. Mater.* **7**, 033402 (2023).
- [12] X. Wang et al., Electrical and magnetic anisotropies in van der Waals multiferroic CuCrP₂S₆, *Nat Commun* **14**, 1 (2023).
- [13] D. Upreti, R. Basnet, M. M. Sharma, S. K. Chhetri, G. Acharya, M. R. U. Nabi, J. Sakon, M. Benamara, M. Mortazavi, and J. Hu, Medium-Entropy Engineering of Magnetism in Layered Antiferromagnet CuxNi₂(1-x)Cr_xP₂S₆, *Advanced Functional Materials* **35**, 2418722 (2025).

- [14] Y. Peng et al., Magnetic Structure and Metamagnetic Transitions in the van der Waals Antiferromagnet CrPS₄, *Advanced Materials* **32**, 2001200 (2020).
- [15] M. A. McGuire, G. Clark, S. KC, W. M. Chance, G. E. Jellison, V. R. Cooper, X. Xu, and B. C. Sales, Magnetic behavior and spin-lattice coupling in cleavable van der Waals layered CrCl₃ crystals, *Phys. Rev. Mater.* **1**, 014001 (2017).
- [16] E. J. Telford et al., Layered Antiferromagnetism Induces Large Negative Magnetoresistance in the van der Waals Semiconductor CrSBr, *Advanced Materials* **32**, 2003240 (2020).
- [17] B. Kuhlow, Magnetic Ordering in CrCl₃ at the Phase Transition, *Physica Status Solidi (a)* **72**, 161 (1982).
- [18] A. Scheie, M. Ziebel, D. G. Chica, Y. J. Bae, X. Wang, A. I. Kolesnikov, X. Zhu, and X. Roy, Spin Waves and Magnetic Exchange Hamiltonian in CrSBr, *Advanced Science* **9**, 2202467 (2022).
- [19] J. L. Lado and J. Fernández-Rossier, On the origin of magnetic anisotropy in two dimensional CrI₃, *2D Mater.* **4**, 035002 (2017).
- [20] M. Suzuki et al., Magnetic anisotropy of the van der Waals ferromagnet Cr₂Ge₂Te₆ studied by angular-dependent x-ray magnetic circular dichroism, *Phys. Rev. Res.* **4**, 013139 (2022).
- [21] D.-H. Kim, K. Kim, K.-T. Ko, J. Seo, J. S. Kim, T.-H. Jang, Y. Kim, J.-Y. Kim, S.-W. Cheong, and J.-H. Park, Giant Magnetic Anisotropy Induced by Ligand LS Coupling in Layered Cr Compounds, *Phys. Rev. Lett.* **122**, 207201 (2019).
- [22] S. Calder, A. V. Haglund, Y. Liu, D. M. Pajerowski, H. B. Cao, T. J. Williams, V. O. Garlea, and D. Mandrus, Magnetic structure and exchange interactions in the layered semiconductor CrPS₄, *Phys. Rev. B* **102**, 024408 (2020).
- [23] D. Khomskii, *Transition Metal Compounds* (Cambridge University Press, 2014).
- [24] I. Lee, F. G. Utermohlen, D. Weber, K. Hwang, C. Zhang, J. van Tol, J. E. Goldberger, N. Trivedi, and P. C. Hammel, Fundamental Spin Interactions Underlying the Magnetic Anisotropy in the Kitaev Ferromagnet CrI₃, *Phys. Rev. Lett.* **124**, 017201 (2020).
- [25] J. Si, S. Liu, B. Wang, C. Wang, F. Ren, Y. Jia, and J.-H. Cho, *Contrasting Magnetic Anisotropy in CrCl₃ and CrBr₃: A First-Principles Study*, arXiv:2509.13824.
- [26] C. L. Saiz, J. A. Delgado, J. van Tol, T. Tartaglia, F. Tafti, and S. R. Singamaneni, 2D correlations in the van der Waals ferromagnet CrBr₃ using high frequency electron spin resonance spectroscopy, *Journal of Applied Physics* **129**, 233902 (2021).

- [27] J. Zeisner, K. Mehlawat, A. Alfonsov, M. Roslova, T. Doert, A. Isaeva, B. Büchner, and V. Kataev, Electron spin resonance and ferromagnetic resonance spectroscopy in the high-field phase of the van der Waals magnet CrCl₃, *Phys. Rev. Mater.* **4**, 064406 (2020).
- [28] D. MacNeill, J. T. Hou, D. R. Klein, P. Zhang, P. Jarillo-Herrero, and L. Liu, Gigahertz Frequency Antiferromagnetic Resonance and Strong Magnon-Magnon Coupling in the Layered Crystal CrCl₃, *Phys. Rev. Lett.* **123**, 047204 (2019).
- [29] J. Zeisner, A. Alfonsov, S. Selzer, S. Aswartham, M. P. Ghimire, M. Richter, J. van den Brink, B. Büchner, and V. Kataev, Magnetic anisotropy and spin-polarized two-dimensional electron gas in the van der Waals ferromagnet Cr₂Ge₂Te₆, *Phys. Rev. B* **99**, 165109 (2019).
- [30] F. Moro, S. Ke, A. G. del Águila, A. Söll, Z. Sofer, Q. Wu, M. Yue, L. Li, X. Liu, and M. Fanciulli, Revealing 2D Magnetism in a Bulk CrSBr Single Crystal by Electron Spin Resonance, *Advanced Functional Materials* **32**, 2207044 (2022).
- [31] S. Khan, C. W. Zollitsch, D. M. Arroo, H. Cheng, I. Verzhbitskiy, A. Sud, Y. P. Feng, G. Eda, and H. Kurebayashi, Spin dynamics study in layered van der Waals single-crystal Cr₂Ge₂Te₆, *Phys. Rev. B* **100**, 134437 (2019).
- [32] S. Chehab, J. Amiell, P. Biensan, and S. Flandrois, Two-dimensional ESR behaviour of CrCl₃, *Physica B: Condensed Matter* **173**, 211 (1991).
- [33] T. Kampfrath, A. Sell, G. Klatt, A. Pashkin, S. Mährlein, T. Dekorsy, M. Wolf, M. Fiebig, A. Leitenstorfer, and R. Huber, Coherent terahertz control of antiferromagnetic spin waves, *Nature Photon* **5**, 31 (2011).
- [34] S. Baierl et al., Terahertz-Driven Nonlinear Spin Response of Antiferromagnetic Nickel Oxide, *Phys. Rev. Lett.* **117**, 197201 (2016).
- [35] T. M. J. Cham, S. Karimeddiny, A. H. Dismukes, X. Roy, D. C. Ralph, and Y. K. Luo, Anisotropic Gigahertz Antiferromagnetic Resonances of the Easy-Axis van der Waals Antiferromagnet CrSBr, *Nano Lett.* **22**, 6716 (2022).
- [36] W. F. Io et al., Direct observation of intrinsic room-temperature ferroelectricity in 2D layered CuCrP₂S₆, *Nat Commun* **14**, 1 (2023).
- [37] K. Cho, S. Lee, R. Kalaivanan, R. Sankar, K.-Y. Choi, and S. Park, Tunable Ferroelectricity in Van der Waals Layered Antiferroelectric CuCrP₂S₆, *Advanced Functional Materials* **32**, 2204214 (2022).

- [38] V. Sharma, E. Negusse, R. Kumar, and R. C. Budhani, Ferromagnetic resonance measurement with frequency modulation down to 2 K, *Review of Scientific Instruments* **95**, 063902 (2024).
- [39] M. Dalal, *A Textbook of Inorganic Chemistry – Volume 1* (Dalal Institute, 2017).
- [40] J. Zhang et al., Unveiling Electronic Correlation and the Ferromagnetic Superexchange Mechanism in the van der Waals Crystal CrSiTe₃, *Phys. Rev. Lett.* **123**, 047203 (2019).
- [41] R. Basnet, D. Upreti, T. Patel, S. Karki Chhetri, G. Acharya, M. R. U. Nabi, M. M. Sharma, J. Sakon, M. Mortazavi, and J. Hu, Field-induced spin polarization in the lightly Cr-substituted layered antiferromagnet NiPS₃, *Phys. Rev. B* **109**, 184405 (2024).
- [42] P. Luo, S. Qu, Z. Zhou, W. Li, L. Gao, H. Jiang, X. Liu, and Y. Zheng, Magnetism and magnetoelectric coupling in the van der Waals antiferromagnet CuCr_{1-x}V_xP₂S₆, *Phys. Rev. B* **111**, 224408 (2025).
- [43] J. Tang et al., Raman Fingerprints of Phase Transitions and Ferroic Couplings in van der Waals Multiferroic CuCrP₂S₆, *J. Phys. Chem. Lett.* **16**, 4336 (2025).
- [44] M. A. Susner, R. Rao, A. T. Pelton, M. V. McLeod, and B. Maruyama, Temperature-dependent Raman scattering and x-ray diffraction study of phase transitions in layered multiferroic CuCrP₂S₆, *Phys. Rev. Mater.* **4**, 104003 (2020).
- [45] M. Hong, L. Dai, H. Hu, and C. Li, Structural, ferroelectric, and electronic transitions in the van der Waals multiferroic material CuCrP₂S₆ under high temperature and high pressure, *Phys. Rev. B* **110**, 144103 (2024).
- [46] P. Colombet, A. Leblanc, M. Danot, and J. Rouxel, Structural aspects and magnetic properties of the lamellar compound Cu_{0.50}Cr_{0.50}PS₃, *Journal of Solid State Chemistry* **41**, 174 (1982).
- [47] C. B. Park, A. Shahee, K.-T. Kim, D. R. Patil, S. A. Guda, N. Ter-Oganessian, and K. H. Kim, Observation of Spin-Induced Ferroelectricity in a Layered van der Waals Antiferromagnet CuCrP₂S₆, *Advanced Electronic Materials* **8**, 2101072 (2022).
- [48] D. J. Goossens and T. J. Hicks, The magnetic phase diagram of Mn_xZn_{1-x}PS₃, *J. Phys.: Condens. Matter* **10**, 7643 (1998).
- [49] R. Basnet, A. Wegner, K. Pandey, S. Stormont, and J. Hu, Highly sensitive spin-flop transition in antiferromagnetic van der Waals material MPS₃(M = Ni and Mn), *Phys. Rev. Materials* **5**, 064413 (2021).

- [50] F. Pei et al., Surface-Sensitive Detection of Magnetic Phase Transition in Van Der Waals Magnet CrSBr, *Advanced Functional Materials* **34**, 2309335 (2024).
- [51] F. Keffer and C. Kittel, Theory of Antiferromagnetic Resonance, *Phys. Rev.* **85**, 329 (1952).
- [52] G. Clemente, M. Moret, A. G. del Águila, M. Hussain, Z. Sofer, J. Zhou, X. Liu, M. Fanciulli, and F. Moro, Electron spin resonance on a 2D van der Waals CrBr₃ uniaxial ferromagnet, *J. Appl. Phys.* **133**, 034301 (2023).
- [53] C. Kittel, Theory of Antiferromagnetic Resonance, *Phys. Rev.* **82**, 565 (1951).
- [54] S. Greenwald, Changes in Lattice Constants of Cr₂O₃ near the Curie Temperature, *Nature* **168**, 379 (1951).
- [55] R. J. Sokolewicz, M. Baglai, I. A. Ado, M. I. Katsnelson, and M. Titov, Gilbert damping in two-dimensional metallic antiferromagnets, *Phys. Rev. B* **109**, 134427 (2024).
- [56] H. Xu et al., Electrical detection of spin pumping in van der Waals ferromagnetic Cr₂Ge₂Te₆ with low magnetic damping, *Nat Commun* **14**, 3824 (2023).
- [57] T. Zhang, Y. Chen, Y. Li, Z. Guo, Z. Wang, Z. Han, W. He, and J. Zhang, Laser-induced magnetization dynamics in a van der Waals ferromagnetic Cr₂Ge₂Te₆ nanoflake, *Appl. Phys. Lett.* **116**, 223103 (2020).
- [58] M. Strungaru, Model of Magnetic Damping and Anisotropy at Elevated Temperatures: Application to Granular FePt Films, *Phys. Rev. Appl.* **14**, (2020).
- [59] R. Dally, Short-Range Correlations in the Magnetic Ground State of Na₄Ir₃O₈, *Phys. Rev. Lett.* **113**, (2014).
- [60] X. F. Miao, Short-range magnetic correlations and spin dynamics in the paramagnetic regime of (Mn,Fe)₂(P,Si), *Phys. Rev. B* **94**, (2016).
- [61] G. T. Lin et al., Tricritical behavior of the two-dimensional intrinsically ferromagnetic semiconductor CrGeTe₃, *Phys. Rev. B* **95**, 245212 (2017).
- [62] B. Liu, Y. Zou, L. Zhang, S. Zhou, Z. Wang, W. Wang, Z. Qu, and Y. Zhang, Critical behavior of the quasi-two-dimensional semiconducting ferromagnet CrSiTe₃, *Sci Rep* **6**, 33873 (2016).